ACSNANO

www.acsnano.org

ARTICLE

Scanning Tunneling Microscopy and Spectroscopy of Air Exposure Effects on Molecular Beam Epitaxy Grown WSe_2 Monolayers and Bilayers

Jun Hong Park,[†,⬡] Suresh Vishwanath,[§,#,⬡] Xinyu Liu,[¶] Huawei Zhou,[⊥] Sarah M. Eichfeld,[Ω] Susan K. Fullerton-Shirey,[△] Joshua A. Robinson,[Ω] Randall M. Feenstra,[□] Jacek Furdyna,[¶] Debdeep Jena,[§,#,∥] Huili Grace Xing,[*,§,#,∥] and Andrew C. Kummel[*,†,‡]

[†]Materials Science & Engineering Program and [‡]Department of Chemistry and Biochemistry, University of California, San Diego, La Jolla, California 92093,United States

[§]School of Electrical and Computer Engineering, [⊥]School of Chemical and Biomolecular Engineering, and [∥]Department of Materials Science and Engineering, Cornell University, Ithaca, New York 14850, United States

[#]Electrical Engineering Department and [¶]Physics Department, University of Notre Dame, Notre Dame, Indiana 46556, United States

[□]Department of Physics, Carnegie Mellon University, Pittsburgh, Pennsylvania 15213, United States

[Ω]Department of Materials Science and Engineering, Pennsylvania State University, University Park, Pennsylvania 16802, United States

[△]Department of Chemical and Petroleum Engineering, University of Pittsburgh, Pittsburgh, Pennsylvania 15213, United States

Supporting Information

ABSTRACT: The effect of air exposure on 2H-WSe_2/HOPG is determined *via* scanning tunneling microscopy (STM). WSe_2 was grown by molecular beam epitaxy on highly oriented pyrolytic graphite (HOPG), and afterward, a Se adlayer was deposited *in situ* on WSe_2/HOPG to prevent unintentional oxidation during transferring from the growth chamber to the STM chamber. After annealing at 773 K to remove the Se adlayer, STM images show that WSe_2 layers nucleate at both step edges and terraces of the HOPG. Exposure to air for 1 week and 9 weeks caused air-induced adsorbates to be deposited on the WSe_2 surface; however, the band gap of the terraces remained unaffected and nearly identical to those on decapped WSe_2. The air-induced adsorbates can be removed by annealing at 523 K. In contrast to WSe_2 terraces, air exposure caused the edges of the WSe_2 to oxidize and form protrusions, resulting in a larger band gap in the scanning tunneling spectra compared to the terraces of air-exposed WSe_2 monolayers. The preferential oxidation at the WSe_2 edges compared to the terraces is likely the result of dangling edge bonds. In the absence of air exposure, the dangling edge bonds had a smaller band gap compared to the terraces and a shift of about 0.73 eV in the Fermi level toward the valence band. However, after air exposure, the band gap of the oxidized WSe_2 edges became about 1.08 eV larger than that of the WSe_2 terraces, resulting in the electronic passivation of the WSe_2.

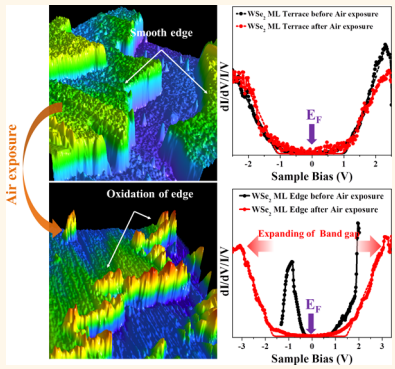

KEYWORDS: *WSe_2, STM, STS, molecular beam epitaxy, air exposure, oxidation*

Layered transition metal dichalcogenides (TMDs) have attracted widespread attention in the scientific community for electronic device applications because their electrical properties can range from superconducting to metallic to semiconducting with a band gap spanning from far IR to near UV. TMDs exhibit distinct layer dependence in their electronic and optical properties, including band gap (*e.g.*, monolayer (ML) TMDs have larger band gaps than multilayer), indirect-to-direct band gap crossover, harmonic generation, valley pseudospin effects, *etc.*[1−8] Furthermore, the two-dimensional (2D) topology of these layered materials enables heterojuction stacking without inducing lattice mismatch and strain between the layers. This feature makes possible the fabrication of transistors and diodes scaled to

Received: December 7, 2015
Accepted: March 18, 2016
Published: March 18, 2016

DOI: 10.1021/acsnano.5b07698
ACS Nano 2016, 10, 4258−4267

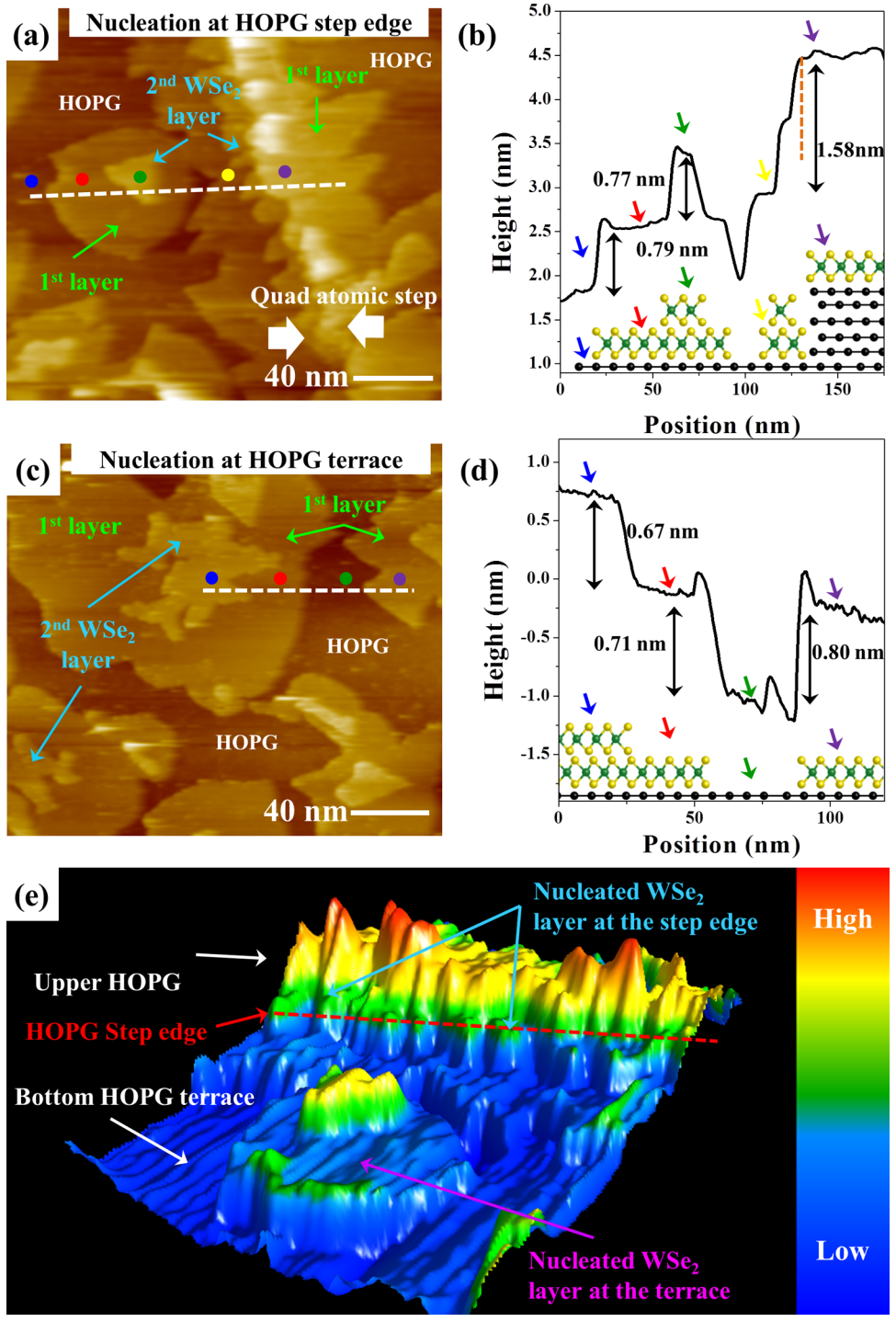

Figure 1. Large-area STM images of WSe_2 growth on HOPG and schematic diagrams. (a) Large-area STM image of ML and BL WSe_2 grown along the step edge of HOPG (V_{sample}: 2 V, I_T: 20 pA). (b) Corresponding line trace along the dashed line in (a). In the corresponding schematic, the height of ML WSe_2 is assumed to equal 0.7 nm, while the height of ML carbon is assumed to equal 0.3 nm. (c) Large-area STM image of ML and BL WSe_2 grown at the step edge of HOPG (V_{sample}: 2 V, I_T: 20 pA). (d) Corresponding line trace along the dashed line in (c). (e) Three-dimensional STM image of a WSe_2 flake on HOPG, corresponding to (a).

atomic thicknesses with tunable band gaps and excitonic effects.[9−11] Among the TMDs, WSe_2 is interesting because of its electronic properties such as a large spin−orbit coupling of >400 meV,[12] valley coherence,[13] small direct−indirect gap crossover energy observed by photoluminescence (PL),[14] transistors with controlled ambipolar behavior,[3] moderate ML mobility of ∼250 cm^2/V s, and bulk mobility as high as 500 cm^2/V s.[1,3,15]

Various TMD growth methods, characterization of physical properties, and device applications have been intensively pursued by multiple research groups. Initial investigations on 2D TMDs focused on exfoliated bulk crystals that were naturally formed or grown by chemical vapor transport (CVT) or chemical vapor deposition (CVD).[16−18] Molecular beam epitaxy (MBE) has been employed more recently to grow high-

DOI: 10.1021/acsnano.5b07698
ACS Nano 2016, 10, 4258−4267

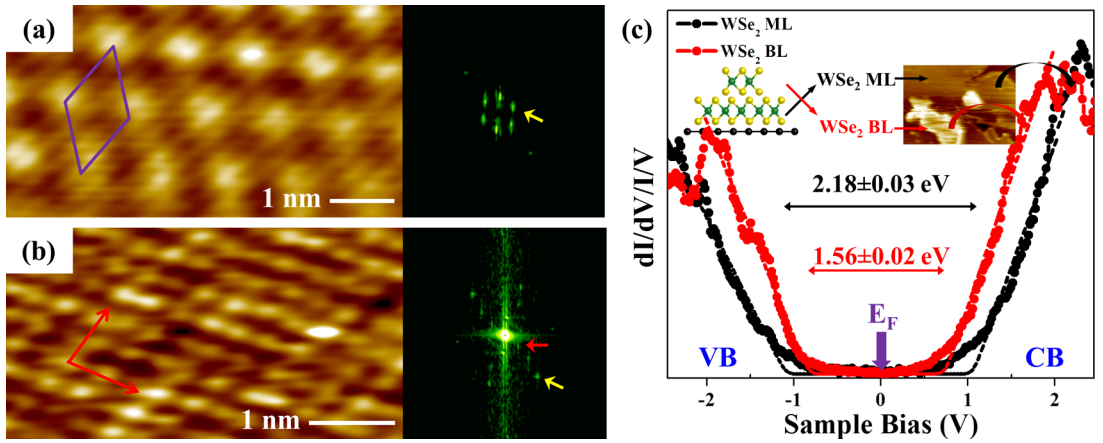

Figure 2. UHV atomic resolution STM image and STS of decapped MBE WSe_2 on HOPG. (a) STM image of hexagonal moiré pattern and corresponding Fourier transform (V_{sample}: 2 V, I_T: 60 pA). (b) Atomically resolved STM image showing hexagonal atomic arrays of Se atoms in WSe_2 and corresponding Fourier transform (V_{sample}: 1.5 V, I_T: 80 pA). As the sample bias is changed, the moiré pattern disappears in (b). (c) $(dI/dV)/(I/V)$ of ML (black) and bilayer (red) WSe_2, showing electronic band gaps of 2.18 ± 0.03 eV for ML WSe_2 and 1.56 ± 0.02 eV for BL WSe_2.

purity, electronic grade crystals of 2D materials, such as $MoSe_2$, $HfSe_2$, and SnS.[19−23]

To realize the potential applications of layered TMDs, such as optoelectronic or logic devices, layered TMD materials are typically exposed to ambient air during device fabrication; therefore, it is critical to understand the effect of air exposure on the structural and electronic properties of layered TMDs. However, studies on the air stability of TMD materials are rare,[24] and the effect of air on the surfaces properties, such as the morphology or band structure, has not been fully understood at the atomic scale.

In the present study, the material properties of MBE-grown WSe_2 are characterized on the atomic scale by scanning tunneling microscopy (STM) and scanning tunneling spectroscopy (STS) at 100 K before and after air exposure, thereby elucidating the effects of air exposure on the morphology and electronic band gap of WSe_2. WSe_2 was grown on highly oriented pyrolytic graphite (HOPG) *via* MBE using elemental sources in ultrahigh vacuum (UHV), after which a Se capping layer was deposited *in situ* on the WSe_2/HOPG to prevent unintentional oxidation of the WSe_2 surface during transfer from the MBE to the UHV STM. After the Se-capped WSe_2/HOPG sample was transferred, the Se capping layer was sublimated by annealing at 773 K in the UHV STM. On the basis of the STM imaging, a very low defect density in the MBE WSe_2 is observed; this low density can be attributed to growth in high vacuum using high-purity elemental sources. The electronic band gap (E_g) was determined for ML and bilayer (BL) WSe_2 using STS.[20,25] Exposure of the MBE WSe_2/HOPG to the ambient air induced oxidation of the edges of WSe_2, as measured by STM and STS, while the terraces of WSe_2 remained nearly unaffected.

RESULTS AND DISCUSSION

The STM images in Figure 1 show that both HOPG step edges and terraces provide nucleation sites for WSe_2 growth. In Figure 1a, nucleation and growth at a multiatomic step edge of HOPG are shown. Although some islands of WSe_2 grow on the terrace of HOPG, there is a complete coverage of WSe_2 along the HOPG step edges, forming "sawtooth-shaped domains", indicated by the white arrows in Figure 1a. Once WSe_2 is initially nucleated at both the upper and lower HOPG step edges, each WSe_2 layer grows laterally, propagating from the HOPG step edges to the internal HOPG basal planes. The position of this HOPG step edge is marked with a dashed orange line in Figure 1b. The height of the deposited WSe_2 is 0.79 ± 0.02 nm, consistent with the three-atomic-layer (Se−W−Se) thickness of single ML, as shown in the line trace of Figure 1b.[3] Comparing the height of ML WSe_2 on the upper HOPG terrace (purple arrow) to the height of ML WSe_2 on the lower HOPG terrace (yellow arrow), a 1.58 ± 0.03 nm height difference is calculated (Figure 1b), indicating that a five-carbon-atomic-layer HOPG step edge nucleated the WSe_2 growth. This is also illustrated in the schematic diagram superimposed with the line scan corresponding to the dashed line in Figure 1a. Additional information regarding the MBE growth and characterization using reflection high-energy electron diffraction (RHEED) and Raman spectroscopy is provided in Figure S1 of the Supporting Information.

The step flow growth of WSe_2 at the HOPG step edges is not the only growth mode that occurs during MBE growth of WSe_2. Nucleation of WSe_2 can also occur on terraces of HOPG, as shown in Figure 1c and d. In Figure 1c, large islands of WSe_2 ML with variable lateral size (40 to 100 nm diameter) are observed on the HOPG terrace, likely facilitated by defects present on the HOPG terrace, and BL growth is initiated at nearly the center of the WSe_2 ML islands, as indicated by the light blue arrows. The line trace shown in Figure 1d indicates a layer height of 0.83 ± 0.01 nm, consistent with the three-atomic-layer (Se−W−Se) ML thickness. Statistically, approximately 56% of nucleated WSe_2 MLs occur at the HOPG step edge, with the remainder nucleating on the HOPG terraces. In summary, both HOPG step edges and terraces can provide nucleation sites for WSe_2, as shown in the three-dimensional STM image in Figure 1e.

The MBE-deposited WSe_2 layer has a hexagonal structure and low defect density, evident in the STM images in Figure 2. In Figure 2a, STM image shows the moiré pattern of ML WSe_2. The moiré pattern is observed because the electron orbitals of WSe_2 and HOPG overlap, resulting in periodic potential wells that give rise to a hexagonal array of protrusions in the STM images and corresponding dots in the Fourier transform (FT).[26,27] Based on the moiré pattern, the rotation angle is

DOI: 10.1021/acsnano.5b07698
ACS Nano 2016, 10, 4258−4267

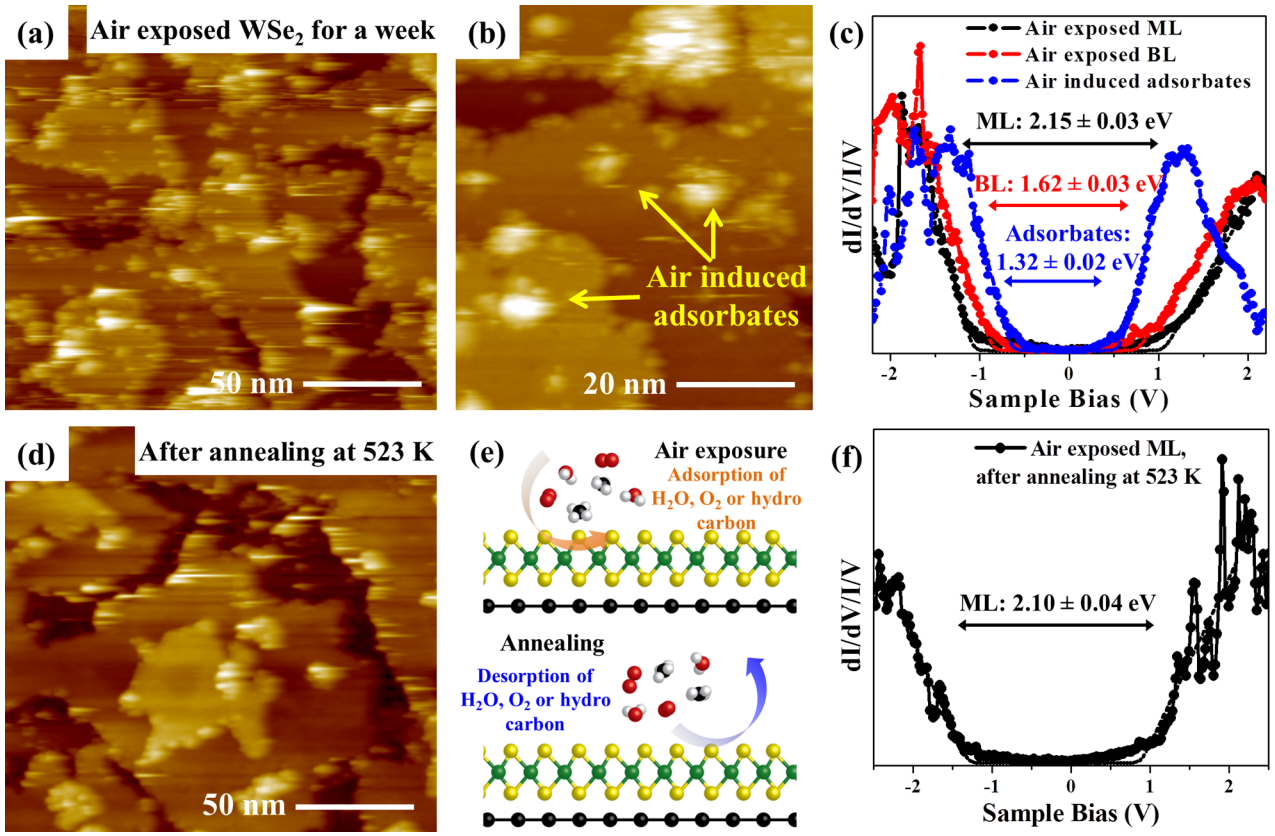

Figure 3. UHV STM image of WSe_2/HOPG after air exposure for 1 week. (a) Large-area STM image of the air-exposed WSe_2 surface (V_{sample}: 2 V, I_t: 10 pA) without annealing. (b) Expanded STM image of the WSe_2 surface exposed to air for 1 week (V_{sample}: 2 V, I_t: 20 pA). Air-induced adsorbates are marked by yellow arrows. (c) STS of air-exposed ML and BL WSe_2 and air-induced adsorbates. (d) STM image of air-exposed WSe_2 surface (V_{sample}: 2 V, I_t: 10 pA), after annealing at 523 K for 30 min. (e) Schematic of the adsorption and annealing induced desorption of air-induced adsorbates. (f) STS of air-exposed ML WSe_2 after annealing at 523 K for 30 min.

calculated to be ~2°; the details of this calculation are described in the Supporting Information. The atomic resolution STM image and the associated FT image in Figure 2b reveal hexagonal arrays of the top Se layer of the three atomic planes in WSe_2. Although each atom has a different local density of states (LDOS), as shown by different brightness in the STM image, noticeable point defects or dislocations are not observed. The variation of LDOS can result from different interactions between WSe_2 and carbon atoms or defects states of the HOPG substrate. The lattice parameter of WSe_2 is measured from STM line traces to be 0.32 ± 0.01 nm (Figure S4), in good agreement with previous crystal structure data.[28]

The quasi-particle band gap of ML and BL WSe_2 was measured using STS.[23,29,30] Figure 2c shows the averaged $(dI/dV)/(I/V)$ *versus* V on a basal plane of WSe_2, far away from step edges of the second WSe_2 layer. The differential conductance dI/dV is normalized by dividing by I/V.[31] Each $(dI/dV)/(I/V)$ is averaged from 10 individual dI/dV spectra. After converting into $(dI/dV)/(I/V)$, a fitting method described in previous STM/STS studies was employed to extract the band gap.[31,32] As shown below, the error is reported as the standard error obtained by the fitting process. It is noted that the uncertainties provided by the present fitting in STS are statistical uncertainties, using the least-squares fitting.[33] Therefore, the given uncertainties can be much less than the thermal broadening in STS. Simulated fits to the STS data are included in Figure 2c as the dashed lines. From the dI/dV spectra on ML WSe_2, the conduction band minimum (CBM) is estimated as +1.08 ± 0.02 V, while the valence band maximum (VBM) is estimated as −1.10 ± 0.01 V. Hence, the quasi-particle band gap for ML WSe_2 is determined to be 2.18 ± 0.03 eV, which is close to the reported theoretical value.[29] Employing the same method, the band gap of BL WSe_2 was also obtained; the CBM is positioned at +0.73 ± 0.01 V, while the VBM is located at −0.83 ± 0.01 V. Therefore, the band gap of bilayer WSe_2 is determined to be 1.56 ± 0.02 eV.[14,30,34] It is noted that in all of our measurements of ML and BL the spectra reveal conductance extending from the band edges into the band gap, suggesting some sort of "band tail" states. The origin of this in-gap conductance is unknown at present; it greatly exceeds any effect of Fermi tails at 100 K in the STS measurements, which are fully included in the theoretical fit function.

To investigate the effect of air exposure on WSe_2/HOPG, the sample was removed from the UHV chamber and exposed to ambient air for 1 week. As shown in Figure 3a, air exposure-induced adsorbates, detected as bright features in STM, are present on both the terraces and step edges. As shown in the expanded STM image in Figure 3b, the diameter of the air-induced adsorbates varies from ~1 to ~10 nm. It is reasonable to assume that hydrocarbons, H_2O, and O_2 are adsorbed on the WSe_2 surface during air exposure. By comparing the band gaps measured in Figures 2c and 3c, it is clear that the air-induced adsorbates do not perturb the band structure of the ML and BL WSe_2; the band gaps of air-exposed ML (2.15 ± 0.03 eV) and BL WSe_2 (1.62 ± 0.03 eV) are nearly identical to the band gap

DOI: 10.1021/acsnano.5b07698
ACS Nano 2016, 10, 4258−4267

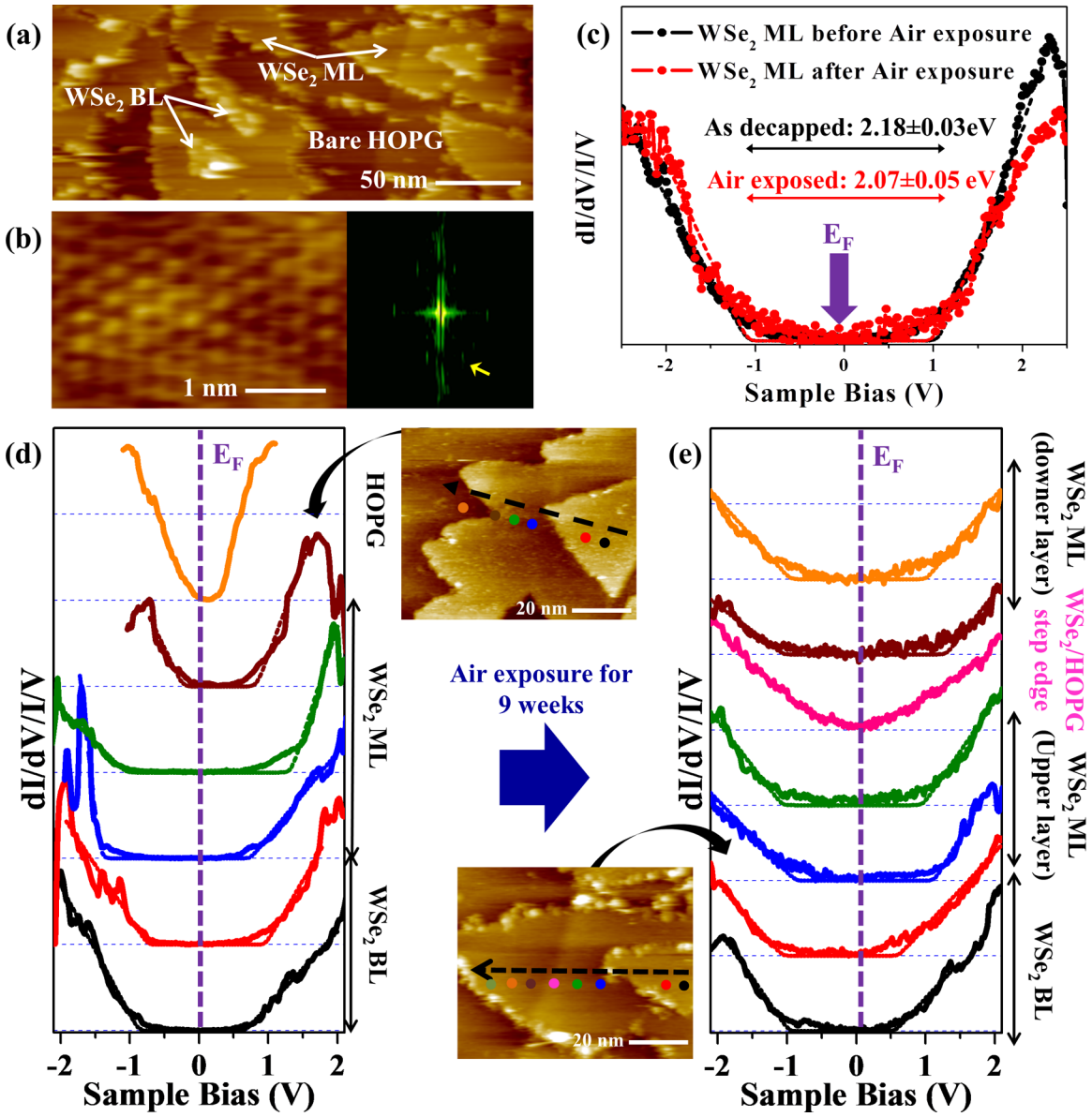

Figure 4. UHV STM image and spatial $(dI/dV)/(I/V)$ spectra of ML and BL WSe_2 before and after air exposure for 9 weeks. The images/spectra taken after air exposure were measured after the sample was annealed in UHV to remove air adsorbates. (a) Large-area STM image of WSe_2 surface exposed to air for 9 weeks (V_{sample}: 2 V, I_t: 15 pA). (b) High-resolution STM image of a WSe_2 ML terrace after air exposure (V_{sample}: −1 V, I_t: 120 pA) and corresponding Fourier transform. (c) STS of a WSe_2 ML before and after air exposure. (d) Subset of $(dI/dV)/(I/V)$ spectra taken along the dashed black line in the STM image in (d), before air exposure. The measured band gaps by STS are 1.54, 1.70, 2.16, 2.23, 1.06, and 0 eV from bottom to top with a maximum error of ±0.04 eV. (e) Subset of $(dI/dV)/(I/V)$ spectra taken along the dashed black line in the STM image in (e), after air exposure. The measured band gaps by STS are 1.51, 1.64, 2.01, 2.05, 0, 2.34, and 2.03 eV from bottom to top with a maximum error of ± 0.05 eV.

of pristine decapped WSe_2. Note that both ML and BL WSe_2 STS spectra were taken at locations within 1 nm of adsorbates. The air-induced adsorbates themselves (blue spectra in Figure 3c) have a smaller band gap than both ML and BL WSe_2; therefore, the adsorbates are more likely to be adsorbed hydrocarbon, H_2O, or O_2 and not oxidation of WSe_2. If the WSe_2 terraces were oxidized, the band gap would be larger (see Figure S11).

The air-induced adsorbates can be removed from the WSe_2 surface by annealing, consistent with reversible adsorption of molecular chemisorbates. As shown in Figure 3d, annealing at 523 K for 30 min induces desorption of most of the adsorbates from the WSe_2 terrace, indicating weak adsorbate binding. Only a few adsorbates remain along the step edge of WSe_2. As shown in Figure 3f, after desorption of adsorbates from the WSe_2 surface, the band gap of ML WSe_2 (2.10 ± 0.02 eV) does not change, compared to the band gap of pristine WSe_2 ML (2.18 ± 0.03 eV), as shown in Figure 2c. It is noted that additional annealing at 723 K for 30 min does not induce topological degradation or perturbation of the band gap, as shown in Figure S9 of the Supporting Information. The proposed adsorption and annealing-induced desorption of hydrocarbons, H_2O, and O_2 on WSe_2 terraces are depicted in the schematic diagram of Figure 3e.

To mimic the asymptotic state of 2D materials during device process and testing, WSe_2/HOPG was also exposed to ambient

DOI: 10.1021/acsnano.5b07698
ACS Nano 2016, 10, 4258−4267

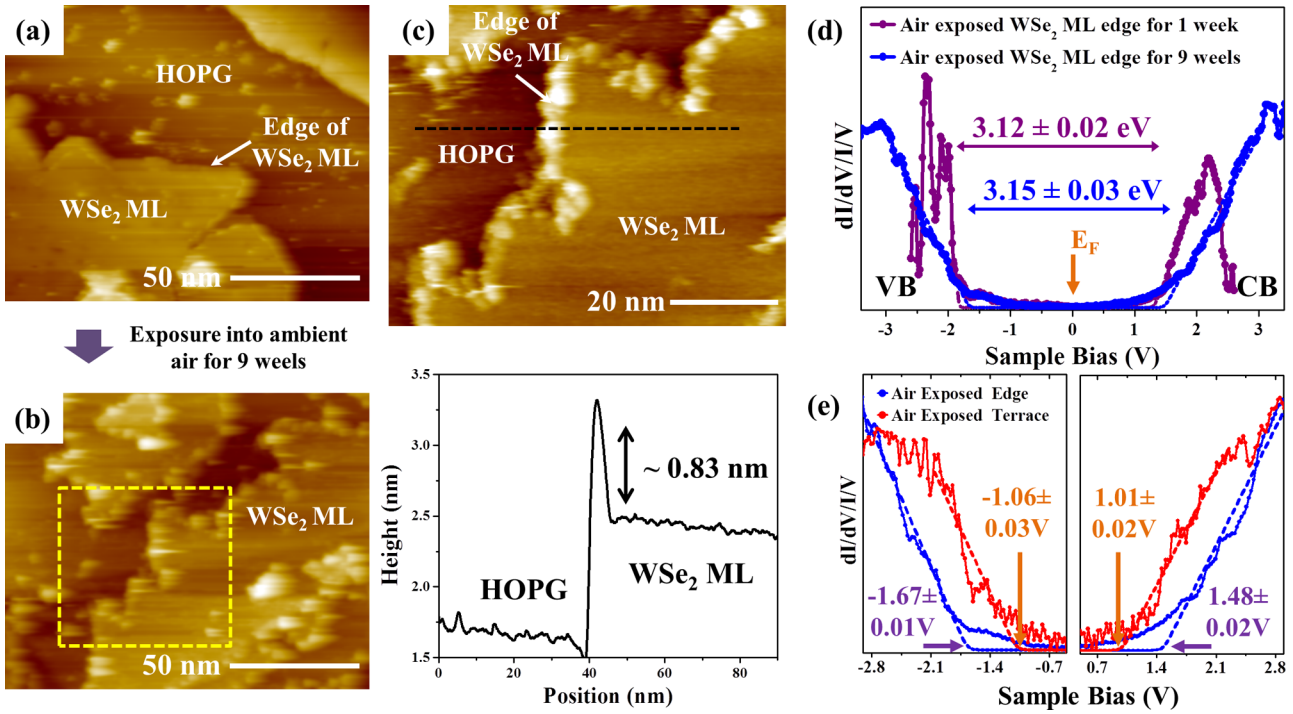

Figure 5. UHV STM image and $(dI/dV)/(I/V)$ of the WSe_2 edge after exposure for 9 weeks to ambient air. The images/spectra taken after air exposure were measured after the sample was annealed in UHV to remove air adsorbates. (a) STM image of decapped WSe_2. Surface (V_{sample}: 2 V, I_t: 20 pA). (b) STM image of air-exposed WSe_2 (V_{sample}: 2 V, I_t: 15 pA). (c) Expanded STM image of the yellow rectangle from Figure 4b and corresponding line trace (V_{sample}: 2 V, I_t: 20 pA). The edge of the WSe_2 ML is decorated by oxidation features. (d) $(dI/dV)/(I/V)$ obtained at the WSe_2 ML edge exposed to air for 1 and 9 weeks (purple and blue curves, respectively). (e) Detailed view of STS from −2.9 to −0.5 V (right) and from 0.5 to 2.9 V (left). The air-exposed WSe_2 ML terrace is included in (e) for comparison of the band gap.

air for 9 weeks. After air exposure, the sample was transferred into an UHV chamber and annealed at 773 K for 20 min to remove ambient hydrocarbons, H_2O, or O_2, thereby enabling stable STM and STS measurements. The large-area STM image in Figure 4a shows the air-exposed ML and BL WSe_2 on HOPG. In the atomic resolution image of Figure 4b, the hexagonal crystal structure of the top Se layer is confirmed and there are no apparent defects, such as vacancies, dislocations, or interstitial impurities. The FT image of Figure 4b displays prominent hexagonal peaks assigned to the topmost Se layer, consistent with the STM image. The band structure of the air-exposed ML WSe_2 is also confirmed by STS in Figure 4c; the VBM is −1.06 ± 0.03 V and the CBM is +1.01 ± 0.02 V, giving a band gap of 2.07 ± 0.05 eV. Comparing the STS of the as-decapped WSe_2 ML terrace (2.18 eV), the band gap of the air exposed WSe_2 ML terraces decreased by only 0.11 ± 0.08 eV; therefore, the band gap of the WSe_2 ML terrace remains nearly constant, even after air exposure for 9 weeks.

Spatial variations in the WSe_2 band structure are detected by measuring the dI/dV spectra from the bilayer WSe_2 to the edge of ML WSe_2 both before and after air exposure. First, the data before air exposure (*i.e.*, as-decapped, Figure 4d) are discussed. The black, dashed line on the STM image indicates the location along which the tunneling spectra were recorded. The black spectrum at the bottom of Figure 4d corresponds to the band structure of BL WSe_2, while the orange spectrum at the top corresponds to the band structure of bare HOPG; the position of the Fermi level (0 V) is marked as the purple dashed line. As the STM tip is moved from BL WSe_2 to ML WSe_2 to HOPG, STS spectra were acquired sequentially. The fitted STS curves are also included as dashed lines in Figure 4d. Starting with BL WSe_2, two dI/dV spectra were recorded (black and red) with a band gap in the range of 1.54 ± 0.02 to 1.70 ± 0.03 eV, consistent with the STS results in Figure 2c. It is noted that the STS curve closest to the edge of the WSe_2 BL (red curve) has a Fermi level slightly shifted toward the valence band. This shift could possibly arise from defect states near the edge of the WSe_2 BL. As the STM tip is moved toward the ML WSe_2 area adjacent to the edge of the BL WSe_2, the Fermi level shifts significantly away from the VBM. The measured band gap of the ML WSe_2 is in the range of 2.16 ± 0.02 to 2.23 ± 0.02 eV, as shown by the blue and green STS curves. At the step edge of the WSe_2 ML, the band gap decreases to 1.06 ± 0.04 eV and a large DOS is observed near the Fermi level. This edge state of WSe_2 will be discussed in further detail below. Beyond the step edge of ML WSe_2, a zero band gap is observed in the $(dI/dV)/(I/V)$ spectrum (orange), consistent with the bare surface of HOPG. The symmetric linear dispersion of the measured LDOS on HOPG is consistent with prior STM/STS results.[18,35,36]

A similar band structure transition from bilayer to monolayer also can be observed on the air-exposed WSe_2/HOPG, Figure 4e. In this case, spectra are also collected along the black dashed line shown in the STM image of Figure 4e. Here, an air-exposed WSe_2 island spans across a monatomic HOPG step edge. Starting from the bottom spectra, two STS curves were obtained on air-exposed BL WSe_2, and both band gaps are similar to the band gap of the as-decapped WSe_2 BL in Figure 4d. As the STM tip moves to the WSe_2 ML near the edge of the bilayer WSe_2, the band gap increases, consistent with that of the WSe_2 ML. However, when the STM tip is positioned on the WSe_2 ML located directly on the monatomic HOPG step edge,

DOI: 10.1021/acsnano.5b07698
ACS Nano 2016, 10, 4258−4267

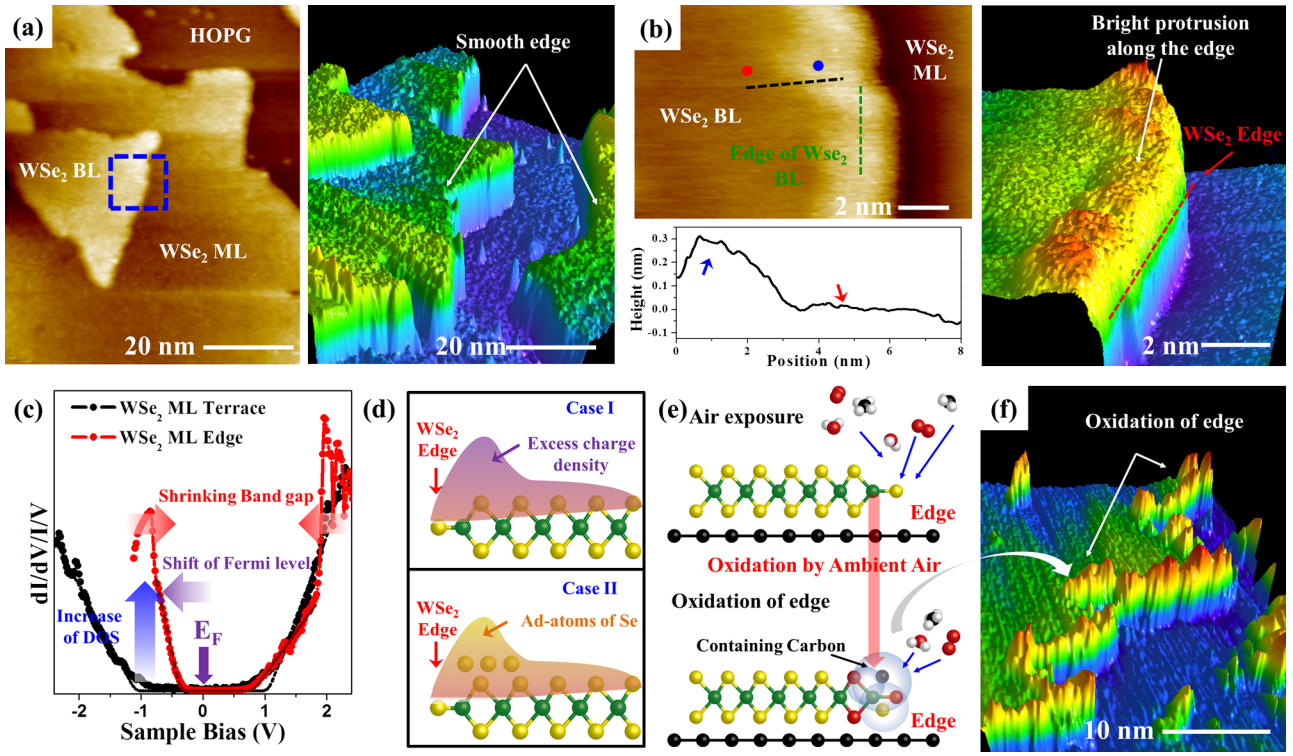

Figure 6. UHV STM and STS of WSe_2 edges and proposed oxidation model in the ambient air. (a) Left: Large-scale STM image of the edge of the WSe_2 ML before air exposure (V_s: 2 V, I_t: 20 pA). Right: 3D rendered STM image showing the smooth edge of the WSe_2 layers. (b) Expanded STM images of the blue rectangle in Figure 5a (V_s: −1 V, I_t: 40 pA) and corresponding line trace along the dash line in Figure 5b. An expanded 3D rendered STM image of the edge of WSe_2 is shown on the right. (c) STS spectra recorded at the edge of the WSe_2 ML and the terrace of the WSe_2 ML, both before air exposure. (d) Proposed schematic of WSe_2 edges before exposure to air. (e) Proposed schematic of oxidation of WSe_2 edges in ambient air. Oxide at the edge contains C and Se (black and yellow balls). (f) 3D rendered STM image of an oxidized edge of WSe_2.

the band gap decreases to nearly 0 eV and a linear dispersion of the band structure is observed (pink curve). It is likely that the electronic structure of the WSe_2 ML is perturbed by the dangling bonds of the underlying HOPG step edge. This localized DOS of the HOPG step edge is explained in Figure S8. When the STM tip is moved far from the WSe_2 ML/HOPG step edge, the STS curves are consistent with those representing the original band structure of the WSe_2 ML. Therefore, the spatially resolved band structure measurements before and after air exposure show that the terraces of the MBE WSe_2 ML and BL appear to be nearly inert to the air exposure.

Although the terraces of WSe_2 are left nearly unaffected upon air exposure and UHV annealing, oxidation of the WSe_2 edges is observed. As seen in Figure 5a, the WSe_2 ML before exposure to ambient air (*i.e.*, as-decapped) has clean and smooth step edges. However, after exposure to the ambient air and subsequent UHV annealing, the edges of the WSe_2 ML are decorated by air-induced protrusions, as seen in Figure 5b, with a height of 0.83 ± 0.03 nm, as shown in a line trace in Figure 5c. These protrusions can also be observed at the edge of the WSe_2 BL after air exposure, as shown in Figure S10.

The STS spectra in Figure 5d and e show that the air-exposed edge states have a larger band gap compared to the air-exposed terraces, consistent with the formation of a metal oxide with a relatively large band gap. In Figure 5d, the air-exposed ML WSe_2 edge for both 1 week (3.12 ± 0.02 eV) and for 9 weeks (3.15 ± 0.03 eV) have nearly identical band gaps. As shown in Figure 5e, the $(dI/dV)/(I/V)$ is displayed for both the air-exposed WSe_2 ML edge and the air-exposed WSe_2 ML terrace for 9 weeks so that the band gaps can be compared. As the position of the STM tip is moved from terrace to edge, the VBM to Fermi level energy increases by 0.61 ± 0.04 V, while the CBM to Fermi level energy increases by 0.47 ± 0.04 V from 0 V; therefore, the band gap of the air-exposed edge is larger by 1.08 ± 0.08 eV than band gap of air-exposed terrace. This 3.15 ± 0.03 eV band gap at the air-exposed edge is very close to the theoretically calculated band gap of monoclinic WO_3 or the band gap of sub 2 nm WO_3 quantum dots.[37−39] Combining STM and STS results, it can be concluded that the air exposure of WSe_2/HOPG induces selective oxidation of the WSe_2 edges.

To better understand the oxidation process in air, the bare WSe_2 edges were characterized with STM and STS before air exposure (*i.e.*, the as-decapped WSe_2). In Figure 6a, typical WSe_2 ML and BL edges are displayed in empty-state STM imaging; both ML and BL possess smooth, clean edges, similar to Figure 5a. A 3D rendered STM image also shows clean and rectangular edges of the WSe_2 layer, without observable corrugation along the edge of the WSe_2. However, a higher resolution filled-state image of the edge of WSe_2 BL in the blue square in Figure 6a reveals a bright rim along the edge, shown as a green dashed line in Figure 6b. The 3D rendered STM image also confirms that the edge contour is higher than the internal terrace. From a filled-state STM image, the line trace indicates the height of the edge contour as 0.28 ± 0.02 nm, which is similar in height to dangling bonds on the Si (001) surface.[40,41] Although similar bright brims are also observed along the step edge of bare HOPG (Figure S8), there are two reasons that the bright brims along the WSe_2 edges cannot

DOI: 10.1021/acsnano.5b07698
ACS Nano 2016, 10, 4258−4267

originate from the HOPG step edges: (1) the bright brims observed at the HOPG step edges are shown in the empty-state imaging and (2) WSe_2 edges are positioned not only at the HOPG step edges but also at the HOPG terrace.

As shown in Figure 6c, two major differences are observed in the STS spectra taken at the edge of WSe_2 compared to bare WSe_2 terraces. First, the DOS at the VB (approximately −1 V sample bias) is increased at the edge of the WSe_2 ML (blue arrow). This increase is consistent with the increased brightness of the terrace edges in the filled-state STM images in Figure 6b. The STS spectrum acquired at the edge indicates a band gap of 1.1 ± 0.04 eV, with the Fermi level located relatively close to the valence band. Comparing the as-decapped WSe_2 edge in Figure 6c with the air-exposed WSe_2 ML edge in Figure 5d, the band gap of the air-exposed edge is increased 3 times from the band gap of the as-decapped edge. These differences in the band structure at the step edges indicate the existence of new electron states.

On the basis of the STM and STS data, two schematic models for these new states along the WSe_2 edge are proposed in Figure 6d. In case I, the dangling bonds from the atoms at the WSe_2 edge might form enhanced VB states, which are observed as a bright corrugation in the filled-state STM image, similar to dangling bonds on the Si(001) surface.[40,41] In case II, dangling bonds cause the condensation of Se adatoms, which form the thin layer at the step edge. Both models share the common feature of electronic edge states along the outmost atoms at the WSe_2 edge. However, the observation of electronic edge state (case 1) is consistent with previous STM measurements and DFT calculations on MoS_2 nanocrystals showing that the edge of MoS_2 has a metallic band structure, resulting in high reactivity with other molecules or catalytic activities.[42−46] Moreover, previous DFT calculations on MoS_2 nanoclusters show that the DOS at edges is larger near the Fermi level than the DOS of terraces in the projected p-orbital DOS.[45] Therefore, it seems most likely that the WSe_2 edge states are due to electronic defects of the edge atoms (case I), rather than an excess Se adatoms (case II).

On the basis of the STM/STS results on WSe_2 edges, together with previous DFT and experimental data, it is hypothesized that the WSe_2 electronic edge states result from dangling bonds that facilitate air-induced reactions; a schematic model of the edge oxidation process is shown in Figure 6e. Prior to oxidation, the WSe_2 edge is depicted as a half-selenided W edge (*i.e.*, W and one Se atom). Although Figure 6e displays only a half-selenided W edge, other variations of the atomic structures at the edge can exist, depending on the size of the WSe_2 flakes or deposition conditions.[43,44,47] In ambient air, the dangling bonds of the outermost atoms are passivated by adsorption of H_2O, O_2, or hydrocarbon molecules. Although both Se and W are expected to oxidize to SeO_x and WO_x, respectively, SeO_x (selenium oxide) has a desorption temperature much less than 773 K,[48,49] and therefore the SeO_x products will desorb during UHV annealing at 773 K, leaving WO_x at the edge. It is noted that the WO_x may not be pure and may contain carbon (C), consistent with contaminated oxide, as shown in Figure 6e, where the C or Se atom (black and yellow ball, respectively) is modeled as being in the edge oxide.[50] Because the oxidized and annealed edge states have high thermal stability, they persist after the UHV anneal and can be detected by STM as protrusions decorating the edges of the WSe_2, as shown in a 3D rendered STM image in Figure 6f. The basic model of air exposure and subsequent annealing forming WO_x at step edges is consistent with all the STM and STS data.

CONCLUSION

Molecular beam epitaxy was used to grow WSe_2 on HOPG, and layers were subsequently characterized by STM and STS. The samples were capped by an excess 20 nm Se adlayer after growth and decapped for STM imaging. High-resolution STM images show almost no observable vacancy defects and dislocations on decapped WSe_2, except near step edges. High-resolution filled-state STM images revealed a distinct corrugation along the as-decapped WSe_2 edges, while STS displayed a narrower band gap and shifted Fermi level toward the valence band compared with locations in the center of the terraces. To investigate effects of air exposure on WSe_2 layers, the WSe_2/HOPG was exposed to ambient air for 1 week and 9 weeks. STM images reveal that the terraces of WSe_2 are nearly unaffected; although air-induced adsorbates are deposited across the WSe_2 surface, the band gap of air-exposed WSe_2 ML is measured as 2.07 ± 0.05 eV, nearly identical to 2.18 ± 0.03 eV prior to air exposure, and atomic resolution STM images display a hexagonal array of the topmost Se layer without noticeable defects after the air exposure and UHV annealing. In contrast, the WSe_2 edge is oxidized by exposure to ambient air, involving a topographic transition along the edge and a large band gap (3.15 ± 0.03 eV) of the edge, as measured by STS. The selective reaction at the step edges results from the existence of dangling bonds at the WSe_2 edge, which was confirmed by STM and STS. The present results suggest air exposure of WSe_2 results in oxidation of the WSe_2 edge, while the terrace of WSe_2 is nearly inert to ambient air; therefore, air oxidation of WSe_2 can potentially passivate the electronic edge states, thus minimizing leakage current or electron−hole recombination *via* the conductive edge states in pristine WSe_2, which is desired in devices.

METHODS

1. Deposition of a WSe_2 Layer on HOPG *via* Molecular Beam Epitaxy in Ultrahigh Vacuum. HOPG substrates were gradually heated to 1073 K over 15 min, held for 20 min at 1073 K, and cooled to the growth temperature of 670 K. Once the growth temperature was stabilized, elemental tungsten (W) from an e-beam source and elemental selenium (Se) from a Knudsen cell were dosed simultaneously to grow WSe_2. The growth conditions were designed based on prior MBE growth studies of $MoSe_2$.[22] A low W flux was employed, confirmed by the RHEED pattern appearance of the first layer of WSe_2 after ∼40 min of growth. The Se flux was maintained at a beam equivalent pressure of 1.1×10^{-7} Torr. After growth, the sample was annealed under a Se flux first at 773 K for 3 min and subsequently at 873 K for 7 min. After annealing, the sample was cooled to 263 K under a Se flux to cap WSe_2 with approximately ∼60 nm of Se to protect against ambient in transport to a separate UHV system for STM measurements.

2. Decapping Procedure of the Se Adlayer on WSe_2/HOPG in a UHV Chamber. The Se-capped WSe_2/HOPG samples, transported in a home-built vacuum case, were introduced into a UHV chamber through a load lock (base pressure: 5×10^{-8} Torr) for performing STM/STS measurements. It is noted that the main and STM chamber were held at $\lesssim 1 \times 10^{-10}$ and $\lesssim 5 \times 10^{-11}$ Torr by ion pumping. Prior to STM and STS measurements, the Se capping layers were sublimated by annealing at 773 K for 3 h; samples were heated to 773 K at a 15 K/min rate. After annealing the samples at 773 K, samples were cooled spontaneously.

3. Scanning Tunneling Microscopy and Spectroscopy in the UHV Chamber. STM imaging and STS measurements were performed by variable-temperature STM in the UHV chamber

DOI: 10.1021/acsnano.5b07698
ACS Nano 2016, 10, 4258−4267

(Omicron. Inc.) at 100 K, using electrochemically etched W tips. After removing the Se capping layers from the WSe_2/HOPG samples, the samples were transferred to the STM stages. Afterward, WSe_2/HOPG samples mounted into the STM stage were cooled to 100 K by liquid nitrogen. The differential tunneling conductance (dI/dV) of WSe_2 was probed by scanning tunneling spectroscopy at 100 K using standard lock-in modulation techniques (lock-in modulation voltage: ΔV_{rms} = 20 mV, f = 500 Hz). In the STM system, the generation of tunneling current between the metal tip and the sample is induced by applying a bias to the sample. Prior to the measurement of all STS spectra, a 2 V sample−tip bias was used in constant current imaging with a 20−30 pA constant current; then the imaging and feedback loop were turned off and an $I-V$ measurement was recorded while varying the tip-to-sample distance.

4. Air Exposure of the WSe_2/HOPG Sample. After verifying the as-decapped WSe_2 surfaces, WSe_2/HOPG samples were transferred from a UHV chamber into ambient air. After 9 weeks, the air-exposed WSe_2/HOPG samples were transferred into a UHV chamber, then annealed at 773 K to remove hydrocarbon and adsorbed H_2O or O_2 for stable STM and STS measurements. STM and STS on the air exposed WSe_2/HOPG samples were performed by the same methods as for the as-decapped samples.

ASSOCIATED CONTENT

Supporting Information

The Supporting Information is available free of charge on the ACS Publications website at DOI: 10.1021/acsnano.5b07698.

RHEED, Raman spectroscopy, and additional STM/STS data (PDF)

AUTHOR INFORMATION

Corresponding Authors

*E-mail: grace.xing@cornell.edu.
*E-mail: akummel@ucsd.edu.

Author Contributions

⬡J. H. Park and S. Vishwanath have contributed equally to this publication.

Author Contributions

S.V., A.C.K., and H.G.X. conceived and designed this experiment. S.V. performed the MBE growth of WSe_2 and RHEED and Raman analysis under the supervision of X.L, J.F., D.J., and H.G.X. S.E. and J.R. provided the epitaxial graphene/SiC sample. J.H.P. performed the STM experiments. J.H.P., R.M.F., and A.C.K. analyzed the STM/STS data. S.K.F.S. and A.C.K. provided the chemical models of air oxidation.

Notes

The authors declare no competing financial interest.

ACKNOWLEDGMENTS

This work is supported by NSF Grant DMR 1207213, NSF Grant ECCS 1433490, NSF Grant DMR14-00432, AFOSR, and LEAST-STARnet, a Semiconductor Research Corporation program, sponsored by MARCO and DARPA and by SRC NRI SWAN.

REFERENCES

(1) Podzorov, V.; Gershenson, M. E.; Kloc, C.; Zeis, R.; Bucher, E. High-Mobility Field-Effect Transistors Based on Transition Metal Dichalcogenides. *Appl. Phys. Lett.* **2004**, *84*, 3301−3303.

(2) Radisavljevic, B.; Radenovic, A.; Brivio, J.; Giacometti, V.; Kis, A. Single-Layer MoS_2 Transistors. *Nat. Nanotechnol.* **2011**, *6*, 147−150.

(3) Fang, H.; Chuang, S.; Chang, T. C.; Takei, K.; Takahashi, T.; Javey, A. High-Performance Single Layered WSe_2 p-FETs with Chemically Doped Contacts. *Nano Lett.* **2012**, *12*, 3788−3792.

(4) Mak, K. F.; He, K. L.; Shan, J.; Heinz, T. F. Control of Valley Polarization in Monolayer MoS_2 by Optical Helicity. *Nat. Nanotechnol.* **2012**, *7*, 494−498.

(5) Chen, Y. F.; Xi, J. Y.; Dumcenco, D. O.; Liu, Z.; Suenaga, K.; Wang, D.; Shuai, Z. G.; Huang, Y. S.; Xie, L. M. Tunable Band Gap Photoluminescence from Atomically Thin Transition-Metal Dichalcogenide Alloys. *ACS Nano* **2013**, *7*, 4610−4616.

(6) Schwarz, S.; Dufferwiel, S.; Walker, P. M.; Withers, F.; Trichet, A. A. P.; Sich, M.; Li, F.; Chekhovich, E. A.; Borisenko, D. N.; Kolesnikov, N. N.; Novoselov, K. S.; Skolnick, M. S.; Smith, J. M.; Krizhanovskii, D. N.; Tartakovskii, A. I. Two-Dimensional Metal-Chalcogenide Films in Tunable Optical Microcavities. *Nano Lett.* **2014**, *14*, 7003−7008.

(7) Li, M.; Esseni, D.; Snider, G.; Jena, D.; Xing, H. G. Single Particle Transport in Two-Dimensional Heterojunction Interlayer Tunneling Field Effect Transistor. *J. Appl. Phys.* **2014**, *115*, 074508.

(8) Zeng, H. L.; Dai, J. F.; Yao, W.; Xiao, D.; Cui, X. D. Valley Polarization in MoS_2 Monolayers by Optical Pumping. *Nat. Nanotechnol.* **2012**, *7*, 490−493.

(9) Lee, C. H.; Lee, G. H.; van der Zande, A. M.; Chen, W. C.; Li, Y. L.; Han, M. Y.; Cui, X.; Arefe, G.; Nuckolls, C.; Heinz, T. F.; Guo, J.; Hone, J.; Kim, P. Atomically Thin p-n Junctions with van der Waals Heterointerfaces. *Nat. Nanotechnol.* **2014**, *9*, 676−681.

(10) Rivera, P.; Schaibley, J. R.; Jones, A. M.; Ross, J. S.; Wu, S. F.; Aivazian, G.; Klement, P.; Seyler, K.; Clark, G.; Ghimire, N. J.; Yan, J. Q.; Mandrus, D. G.; Yao, W.; Xu, X. D. Observation of Long-Lived Interlayer Excitons in Monolayer $MoSe_2$-WSe_2 Heterostructures. *Nat. Commun.* **2015**, *6*, 6242.

(11) Yan, R. S.; Fathipour, S.; Han, Y. M.; Song, B.; Xiao, S. D.; Li, M. D.; Ma, N.; Protasenko, V.; Muller, D. A.; Jena, D.; Xing, H. G. Esaki Diodes in van der Waals Heterojunctions with Broken-Gap Energy Band Alignment. *Nano Lett.* **2015**, *15*, 5791−5798.

(12) Kosmider, K.; Gonzalez, J. W.; Fernandez-Rossier, J. Large Spin Splitting in the Conduction Band of Transition Metal Dichalcogenide Monolayers. *Phys. Rev. B: Condens. Matter Mater. Phys.* **2013**, *88*, 245436.

(13) Jones, A. M.; Yu, H. Y.; Ghimire, N. J.; Wu, S. F.; Aivazian, G.; Ross, J. S.; Zhao, B.; Yan, J. Q.; Mandrus, D. G.; Xiao, D.; Yao, W.; Xu, X. D. Optical Generation of Excitonic Valley Coherence in Monolayer WSe_2. *Nat. Nanotechnol.* **2013**, *8*, 634−638.

(14) Zhao, W. J.; Ribeiro, R. M.; Toh, M. L.; Carvalho, A.; Kloc, C.; Neto, A. H. C.; Eda, G. Origin of Indirect Optical Transitions in Few-Layer MoS_2, WS_2, and WSe_2. *Nano Lett.* **2013**, *13*, 5627−5634.

(15) Fang, H.; Tosun, M.; Seol, G.; Chang, T. C.; Takei, K.; Guo, J.; Javey, A. Degenerate n-Doping of Few-Layer Transition Metal Dichalcogenides by Potassium. *Nano Lett.* **2013**, *13*, 1991−1995.

(16) Nitsche, R.; Bolsterli, H. U.; Lichtensteiger, M. Crystal Growth by Chemical Transport Reactions 0.1. Binary, Ternary, and Mixed-Crystal Chalcogenides. *J. Phys. Chem. Solids* **1961**, *21*, 199−205.

(17) Eichfeld, S. M.; Hossain, L.; Lin, Y. C.; Piasecki, A. F.; Kupp, B.; Birdwell, A. G.; Burke, R. A.; Lu, N.; Peng, X.; Li, J.; Azcatl, A.; McDonnell, S.; Wallace, R. M.; Kim, M. J.; Mayer, T. S.; Redwing, J. M.; Robinson, J. A. Highly Scalable, Atomically Thin WSe_2 Grown *via* Metal-Organic Chemical Vapor Deposition. *ACS Nano* **2015**, *9*, 2080−2087.

(18) Zhang, C. D.; Johnson, A.; Hsu, C. L.; Li, L. J.; Shih, C. K. Direct Imaging of Band Profile in Single Layer MoS_2 on Graphite: Quasiparticle Energy Gap, Metallic Edge States, and Edge Band Bending. *Nano Lett.* **2014**, *14*, 2443−2447.

(19) Wang, W.; Leung, K. K.; Fong, W. K.; Wang, S. F.; Hui, Y. Y.; Lau, S. P.; Chen, Z.; Shi, L. J.; Cao, C. B.; Surya, C. Molecular Beam Epitaxy Growth of High Quality p-Doped SnS van der Waals Epitaxy on a Graphene Buffer Layer. *J. Appl. Phys.* **2012**, *111*, 093520.

(20) Ugeda, M. M.; Bradley, A. J.; Shi, S. F.; da Jornada, F. H.; Zhang, Y.; Qiu, D. Y.; Ruan, W.; Mo, S. K.; Hussain, Z.; Shen, Z. X.; Wang, F.; Louie, S. G.; Crommie, M. F. Giant Bandgap Renormalization and Excitonic Effects in a Monolayer Transition Metal Dichalcogenide Semiconductor. *Nat. Mater.* **2014**, *13*, 1091−1095.

DOI: 10.1021/acsnano.5b07698
ACS Nano 2016, 10, 4258−4267

(21) Yue, R. Y.; Barton, A. T.; Zhu, H.; Azcatl, A.; Pena, L. F.; Wang, J.; Peng, X.; Lu, N.; Cheng, L. X.; Addou, R.; McDonnell, S.; Colombo, L.; Hsu, J. W. P.; Kim, J.; Kim, M. J.; Wallace, R. M.; Hinkle, C. L. $HfSe_2$ Thin Films: 2D Transition Metal Dichalcogenides Grown by Molecular Beam Epitaxy. *ACS Nano* **2015**, *9*, 474−480.
(22) Vishwanath, S.; L, X.; Rouvimov, S.; Mende, P. C; Azcatl, A.; McDonnell, S.; Wallace, R. M; Feenstra, R. M; Furdyna, J. K; Jena, D.; Xing, H. G. Comprehensive Structural and Optical Characterization of MBE grown $MoSe_2$ on Graphite, CaF_2 and Graphene. *2D Mater.* **2015**, *2*, 024007.
(23) Liu, H. J.; Jiao, L.; Xie, L.; Yang, F.; Chen, J. L.; Ho, W. K.; Gao, C. L.; Jia, J. F.; Cui, X. D.; Xie, M. H. Molecular-beam epitaxy of monolayer and bilayer WSe_2: a Scanning Tunneling Microscopy/Spectroscopy Study and Deduction of Exciton Binding Energy. *2D Mater.* **2015**, *2*, 034004.
(24) Chae, S. H.; Jin, Y.; Kim, T. S.; Chung, D. S.; Na, H.; Nam, H.; Kim, H.; Perello, D. J.; Jeong, H. Y.; Ly, T. H.; Lee, Y. H. Oxidation Effect in Octahedral Hafnium Disulfide Thin Film. *ACS Nano* **2016**, *10*, 1309−1316.
(25) Zhang, C.; Chen, Y.; Johnson, A.; Li, M.-Y.; Li, L.-J.; Mende, P. C.; Feenstra, R. M.; Shih, C.-K. Probing Critical Point Energies of Transition Metal Dichalcogenides: Surprising Indirect Gap of Single Layer WSe_2. *Nano Lett.* **2015**, *15*, 6494−6500.
(26) Xue, J. M.; Sanchez-Yamagishi, J.; Bulmash, D.; Jacquod, P.; Deshpande, A.; Watanabe, K.; Taniguchi, T.; Jarillo-Herrero, P.; Leroy, B. J. Scanning Tunnelling Microscopy and Spectroscopy of Ultra-Flat Graphene on Hexagonal Boron Nitride. *Nat. Mater.* **2011**, *10*, 282−285.
(27) Geim, A. K.; Grigorieva, I. V. Van der Waals Heterostructures. *Nature* **2013**, *499*, 419−425.
(28) Brixner, L. H. Preparation and Properties of the Single Crystalline Ab_2-Type Selenides and Tellurides of Niobium, Tantalum, Molybdenum and Tungsten. *J. Inorg. Nucl. Chem.* **1962**, *24*, 257−263.
(29) Ramasubramaniam, A. Large Excitonic Effects in Monolayers of Molybdenum and Tungsten Dichalcogenides. *Phys. Rev. B: Condens. Matter Mater. Phys.* **2012**, *86*, 115409.
(30) Desai, S. B.; Seol, G.; Kang, J. S.; Fang, H.; Battaglia, C.; Kapadia, R.; Ager, J. W.; Guo, J.; Javey, A. Strain-Induced Indirect to Direct Bandgap Transition in Multi layer WSe_2. *Nano Lett.* **2014**, *14*, 4592−4597.
(31) Feenstra, R. M.; Lee, J. Y.; Kang, M. H.; Meyer, G.; Rieder, K. H. Band Gap of the Ge(111)c(2 × 8) Surface by Scanning Tunneling Spectroscopy. *Phys. Rev. B: Condens. Matter Mater. Phys.* **2006**, *73*, 035310.
(32) Feenstra, R. M. Tunneling Spectroscopy of the (110)-Surface of Direct-Gap Iii-V Semiconductors. *Phys. Rev. B: Condens. Matter Mater. Phys.* **1994**, *50*, 4561−4570.
(33) Bevington, P. R.; Robinson, D. K. *Data Reduction and Error Analysis for the Physical Sciences*, 3rd ed.; McGraw-Hill: Boston, 2003.
(34) Yun, W. S.; Han, S. W.; Hong, S. C.; Kim, I. G.; Lee, J. D. Thickness and Strain Effects on Electronic Structures of Transition Metal Dichalcogenides: 2H-M X-2 Semiconductors (M = Mo, W; X = S, Se, Te). *Phys. Rev. B: Condens. Matter Mater. Phys.* **2012**, *85*, 033305.
(35) Matsui, T.; Kambara, H.; Niimi, Y.; Tagami, K.; Tsukada, M.; Fukuyama, H. STS Observations of Landau Levels at Graphite Surfaces. *Phys. Rev. Lett.* **2005**, *94*, 226403.
(36) Li, G. H.; Luican, A.; Andrei, E. Y. Scanning Tunneling Spectroscopy of Graphene on Graphite. *Phys. Rev. Lett.* **2009**, *102*, 176804.
(37) Wang, F. G.; Di Valentin, C.; Pacchioni, G. Electronic and Structural Properties of WO_3: A Systematic Hybrid DFT Study. *J. Phys. Chem. C* **2011**, *115*, 8345−8353.
(38) Ping, Y.; Rocca, D.; Galli, G. Optical Properties of Tungsten Trioxide from First-Principles Calculations. *Phys. Rev. B: Condens. Matter Mater. Phys.* **2013**, *87*, 165203.
(39) Watanabe, H.; Fujikata, K.; Oaki, Y.; Imai, H. Band-Gap Expansion of Tungsten Oxide Quantum Dots Synthesized in Sub-Nano Porous Silica. *Chem. Commun.* **2013**, *49*, 8477−8479.
(40) Schofield, S. R.; Studer, P.; Hirjibehedin, C. F.; Curson, N. J.; Aeppli, G.; Bowler, D. R. Quantum Engineering at the Silicon Surface Using Dangling Donds. *Nat. Commun.* **2013**, *4*, 1645.
(41) Pierucci, D.; Naitabdi, A.; Bournel, F.; Gallet, J. J.; Tissot, H.; Carniato, S.; Rochet, F.; Kohler, U.; Laumann, D.; Kubsky, S.; Silly, M. G.; Sirotti, F. Benzaldehyde on Water-Saturated Si(001): Reaction with Isolated Silicon Dangling Bonds *versus* Concerted Hydrosilylation. *J. Phys. Chem. C* **2014**, *118*, 10005−10016.
(42) Helveg, S.; Lauritsen, J. V.; Laegsgaard, E.; Stensgaard, I.; Norskov, J. K.; Clausen, B. S.; Topsoe, H.; Besenbacher, F. Atomic-Scale Structure of Single-Layer MoS_2 Nanoclusters. *Phys. Rev. Lett.* **2000**, *84*, 951−954.
(43) Lauritsen, J. V.; Kibsgaard, J.; Helveg, S.; Topsoe, H.; Clausen, B. S.; Laegsgaard, E.; Besenbacher, F. Size-Dependent Structure of MoS_2 Nanocrystals. *Nat. Nanotechnol.* **2007**, *2*, 53−58.
(44) Tuxen, A.; Kibsgaard, J.; Gobel, H.; Laegsgaard, E.; Topsoe, H.; Lauritsen, J. V.; Besenbacher, F. Size Threshold in the Dibenzothiophene Adsorption on MoS_2 Nanoclusters. *ACS Nano* **2010**, *4*, 4677−4682.
(45) Tsai, C.; Abild-Pedersen, F.; Norskov, J. K. Tuning the MoS_2 Edge-Site Activity for Hydrogen Evolution *via* Support Interactions. *Nano Lett.* **2014**, *14*, 1381−1387.
(46) Bruix, A.; Füchtbauer, H. G.; Tuxen, A. K.; Walton, A. S.; Andersen, M.; Porsgaard, S.; Besenbacher, F.; Hammer, B.; Lauritsen, J. V. *In Situ* Detection of Active Edge Sites in Single-Layer MoS_2 Catalysts. *ACS Nano* **2015**, *9*, 9322−9330.
(47) Lauritsen, J. V.; Bollinger, M. V.; Laegsgaard, E.; Jacobsen, K. W.; Norskov, J. K.; Clausen, B. S.; Topsoe, H.; Besenbacher, F. Atomic-Scale Insight into Structure and Morphology Changes of MoS_2 Nanoclusters in Hydrotreating Catalysts. *J. Catal.* **2004**, *221*, 510−522.
(48) Waitkins, G. R.; Clark, C. W. Selenium Dioxide - Preparation, Properties, and Use as Oxidizing Agent. *Chem. Rev.* **1945**, *36*, 235−289.
(49) Brooks, L. S. The Vapor Pressures of Tellurium and Selenium. *J. Am. Chem. Soc.* **1952**, *74*, 227−229.
(50) Kirss, R. U.; Meda, L. Chemical Vapor Deposition of Tungsten Oxide. *Appl. Organomet. Chem.* **1998**, *12*, 155−160.

DOI: 10.1021/acsnano.5b07698
ACS Nano 2016, 10, 4258−4267